

A creep model for austenitic stainless steels incorporating cavitation and wedge cracking

S Mahesh

Departments of Mechanical and Aerospace Engineering,
Indian Institute of Technology, Kanpur 208016. India.

E-mail: smahesh@iitk.ac.in

K C Alur

Department of Mechanical Engineering,
Indian Institute of Technology, Kanpur 208016. India.

M D Mathew

Mechanical metallurgy division, Indira Gandhi Center for Atomic Research,
Kalpakkam 603102. India

Abstract. A model of damage evolution in austenitic stainless steels under creep loading at elevated temperatures is proposed. The initial microstructure is idealized as a space-tiling aggregate of identical rhombic dodecahedral grains, which undergo power law creep deformation. Damage evolution in the form of cavitation and wedge-cracking on grain boundary facets is considered. Both diffusion- and deformation-driven grain boundary cavity growth are treated. Cavity and wedge-crack length evolution is derived from an energy balance argument that combines and extends the models of Cottrell [1], Williams [2] and Evans [3]. The time to rupture predicted by the model is in good agreement with published experimental data for a type 316 austenitic stainless steel under uniaxial creep loading. Deformation and damage evolution at the microscale predicted by the present model are also discussed.

Keywords: Austenitic stainless steel, creep, grain boundary sliding, cavitation, wedge-cracking.

Submitted to: *Modeling and simulation in materials science and engineering*

1. Introduction

Under service conditions in high temperature applications, austenitic stainless steel components suffer creep damage leading to eventual creep rupture. In the technologically important homologous temperature range of 0.3–0.5, the creep micromechanism transitions from diffusion-controlled cavitation in the low applied stress

range, through cavitation and wedge cracking in the presence of grain-boundary sliding in the intermediate stress range to transgranular fracture at high applied stresses [4, 5].

The low-stress regime has been extensively investigated, both experimentally and through theory and modeling. Cavities, also called r-type voids, grow by a mechanism of diffusion in this regime. Detailed models of cavity nucleation and growth (e.g., [6, 7, 8, 9, 10, 11, 12, 13, 14]) that capture the effect of lattice diffusion, surface diffusion, boundary diffusion, grain creep and the competition between these mechanisms have been proposed. These models are successful in explaining quantitative experimental data both in pure metals and complex alloys [15]. Constrained cavity growth [16], wherein spatially heterogeneous cavitation must be accommodated by diffusion or creep processes in the surrounding grains, has also been extensively studied [8, 9, 17]. The vast literature concerning diffusion-controlled cavitation, dominant at low stresses, has been reviewed by Kassner and Hayes [18].

In the intermediate stress regime, which is the focus of the present work, deformation-based micromechanisms of creep damage become significant. This has been recognized since the 1950s [19, 20, 21]. Wedge cracks caused by grain boundary sliding were observed and classified by Chang and Grant [19] into types (a), (b) and (c) in coarse-grained aluminum. A relation between grain boundary sliding displacement and wedge-crack length was obtained by Cottrell [1] for type (b) wedge-cracks using energy considerations. Identifying creep rupture with the propagation of a Cottrell wedge-crack across a grain boundary facet, Williams [2] obtained a relation between time to creep-rupture and the minimum creep rate. Evans [3], also using an energy based reasoning, developed a model for cavitation in grain boundaries undergoing grain boundary sliding and used it to compute time to rupture by the mechanism of cavitation. Evans' model does not specify the physical mechanisms underlying cavity nucleation and growth and is therefore not mechanistically rigorous. Developments until about 1980 have been surveyed by Evans [22, Chaps. 3 and 6].

Since then, the works of Lai and Wickens [23], Chen and Argon [24], Zauter *et al* [25] and others have revealed that at least in AISI types 304 and 316 austenitic stainless steels, wedge cracks form by accelerated growth and linkage of elongated cavities, previously called w-type voids, near triple lines. These authors thus established that cavitation underlies the formation of both cavities and wedge cracks. Voiding of grain boundaries is found to be distinctly heterogeneous with high void concentrations observed near triple lines and carbide particles. At intermediate stresses, voids were found to be extended in shape [24], with the extension direction coinciding with the grain boundary sliding direction. These observations strongly suggest the central role of grain boundary sliding in inducing damage.

Creep processes governed by mechanisms of deformation such as grain boundary sliding are, however, not as well-understood as those controlled purely by diffusional micromechanisms. A mechanistically rigorous model that accounts for the role of grain boundary sliding on the unconstrained growth of r-type voids is due to Chen [26]. Chen's model assumes homogeneous distribution of cavities on the grain boundary and is

based on balancing surface and grain boundary diffusional atomic fluxes in the presence of a stress enhancement at the cavity tip. This model however does not specify the volumetric growth rate of the cavity, and neglects the effect of local creep processes in cavity growth [12]. The effect of Dyson [16] constraints on Chen-like cavity growth is also not clear: Riedel [27] predicted diffusional cavitation to be faster than that introduced by constrained grain boundary sliding, whereas Chakraborty and Earthman [28] observed the opposite effect in their numerical simulations.

In a series of works incorporating grain boundary sliding and heterogeneous cavitation by diffusion and creep, Tvergaard, Van der Giessen and Onck [12, 13, 14, 29, 30, 31, 32] have computationally studied cavity growth in a two-dimensional finite element model of a polycrystal comprised of initially hexagonal grains undergoing plane strain creep. The requirement of compatibility between neighboring finite elements automatically enforces Dyson [16] constraints on cavity growth in these models. Both r-type and w-type voids are represented in these models in smeared out form. The failure simulations of Van der Giessen and Tvergaard [13] capture damage development in the form of both cavitation and wedge cracking. Onck and Van der Giessen [29, 30, 32] have developed special finite elements to represent the creeping grain and cavitating grain boundary regions. They have then used these elements to simulate creep failure of both initially undamaged material and material ahead of a dominant crack. A limitation of these works is that acceleration of cavity growth on a grain boundary undergoing rapid sliding, although observed experimentally [24], is not accounted for, because of the limitations of Chen's model noted previously [12]. A lesser limitation of these studies stems from their two dimensional character; constraints are known to be weaker in this case than in three dimensional microstructures [9].

Interest in the intermediate stress regime where deformation-based micromechanisms become significant relative to diffusion-based micromechanisms, has been renewed by the material requirements of the core and structural components of fast breeder nuclear reactors presently under development [33]. Under operating conditions in this application, the stress and temperature in certain components fall within the intermediate stress-regime where the creep micromechanism is grain boundary sliding induced cavitation and wedge-cracking (e.g., see [4, Figure 6]). The microstructural evolution and its influence on the time to creep rupture of nuclear grade austenitic stainless steels, particularly AISI type 316, type 316 LN and alloy D9 has been experimentally characterized extensively [34, 35, 36, 37, 38]. The present work is an effort toward complementing the foregoing experimental work with a micromechanical model of creep damage evolution leading up to creep-rupture in the intermediate stress regime.

In the present work, a model of microscopic creep damage evolution and growth in the form of wedge cracks and cavities is developed. Grains undergo Norton power-law creep deformation. Constrained grain boundary sliding is accounted for using Horton's [39] empirical law. Three micromechanisms of creep damage are explicitly represented in the model. These are cavitation by the mechanism of diffusion, cavitation due to grain boundary sliding and wedge cracking. A mechanistically rigorous well-

developed theory [6, 7, 8, 10, 12] is available for diffusional cavitation and is incorporated into the present model. As noted above, a mechanistically rigorous theory for cavitation by a mechanism of deformation caused by grain boundary sliding is not presently available [12]. In order to account for this mechanism in the intermediate stress regime, cavity and wedge crack growth rates are derived from a free energy argument obtained by unifying and extending those of Cottrell [1], Williams [2] and Evans [3]. In this approach, the free-energy changes caused by diffusional and plastic micromechanisms accompanying cavity or wedge-crack growth are subsumed into the effective surface energy of the cavity or wedge-crack. Analytical expressions are obtained for the damage evolution rates while accounting for their mutual interaction. Time integration of damage evolution rates until pre-defined conditions for macroscopic rupture are satisfied yield the time to rupture.

Section 2 describes the idealized microstructure assumed in the present work, followed by the constitutive assumptions underlying creep deformation of individual grains and grain boundary sliding. Damage evolution rates in the form of wedge cracking and cavitation are then derived. Section 3 compares the model predictions with the experimental measurements of Mathew *et al* [34] and Sasikala *et al* [35] in a nuclear grade AISI type 316 stainless steel. The creep lifetime, stretch at rupture and the microscopic failure mode are found to agree well with experimental observations.

2. Creep damage evolution

2.1. Idealized undeformed microstructure

2.1.1. Tiling by identical grains The undeformed polycrystal microstructure is idealized following Drucker [40] and Dryden [41]. Drucker employed this idealization to study creep of sintered carbides in two-dimensions and Dryden extended it to three-dimensional microstructures. The ideal undeformed microstructure is comprised of an aggregate of rhombic dodecahedral grains, one of which is shown in Fig. 1(a). The rhombic dodecahedron is one of two isohedral Fedorov solids (the other being the cube) capable of tiling three-dimensional space [42]. A part of the space-filling tiling is illustrated in Fig. 1(b). In the tiled configuration, centers of neighboring the rhombic dodecahedra describe a face-centered cubic lattice. Following Dryden [41], we denote the distance between the centers of two neighboring grains by 2κ . It can then be shown that each edge of the polyhedron has a length of

$$\kappa_1 = \sqrt{\frac{3}{2}}\kappa, \quad (1)$$

marked in Fig. 1(a) and that the lengths of the diagonals of each rhombus-shaped facet of the polyhedron are 2κ and $\sqrt{2}\kappa$.

Fig. 2 shows a development of the rhombic dodecahedron of Fig. 1(a), together with the facet numbering convention used throughout. The numbering scheme of Fig. 2 is consistent with the numbering scheme of the visible facets of Fig. 1(a). \mathbf{N}_f denotes the

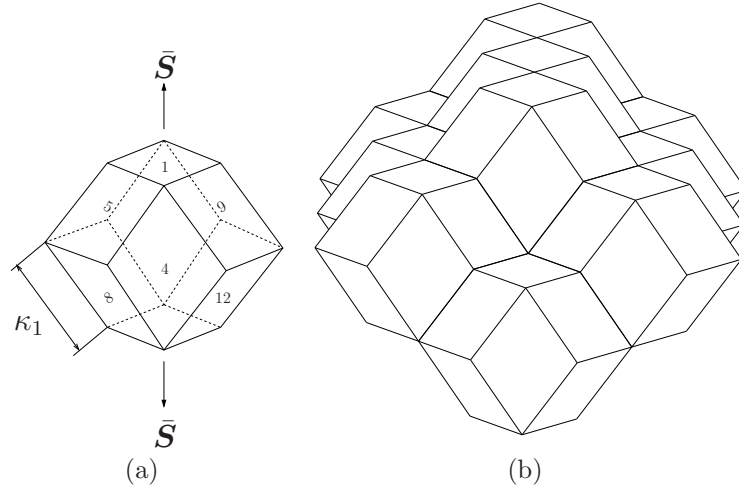


Figure 1. (a) The orientation of a single rhombic dodecahedral ‘grain’ in relation to the tensile loading at constant nominal stress $\bar{\mathbf{S}}$. (b) Part of an infinite space-filling tiling by rhombic dodecahedral grains, which represents the undeformed microstructure.

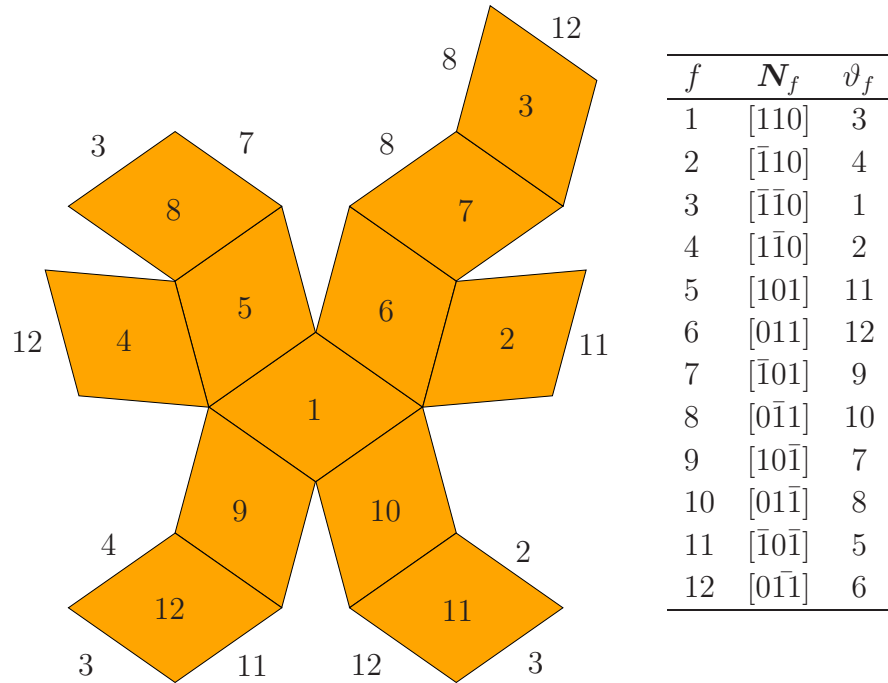


Figure 2. Developed view showing the facets of a rhombic dodecahedron with the facet numbering. Neighbors of a facet that were disconnected during development are indicated outside each facet. Facet normal vector \mathbf{N}_f in Miller-index notation and the number of the opposite facet, v_f are also indicated.

unit outward normal of facet f and ϑ_f denotes the facet that has the opposite outward normal as facet f : $\mathbf{N}_{\vartheta_f} = -\mathbf{N}_f$. Facet f of a rhombic dodecahedron meets facet ϑ_f of its neighboring rhombic dodecahedron. For later use, we also define the set \mathcal{N}_f comprised of the four facets with which facet f shares an edge. Thus, $\mathcal{N}_1 = \{5, 6, 9, 10\}$, etc.

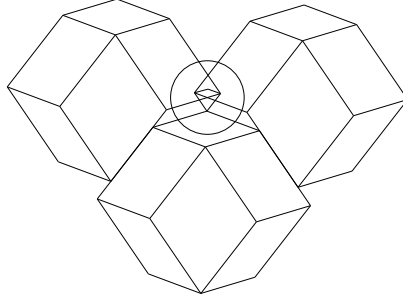


Figure 3. Interpenetration of rigid grains after grain boundary sliding. The region of interpenetration is encircled.

2.1.2. Creep constraints In Dryden's [41] model of creep deformation of sintered ceramics, separation of two grains perpendicular to their common facet is accommodated by the flow of the intergranular fluid phase into the region between the separating grains and grain boundary sliding. In the present material system, however, there is no fluid phase. Therefore, separation of two grains perpendicular to their common facet necessarily entails cavitation or wedge-cracking at the grain boundary between the separating grains. Also, sliding of grains parallel to the common grain boundary is an important mode of damage and deformation in the present material system. Anderson and Rice [9] recognized that grain boundary sliding in a three-dimensional microstructure comprised of rigid grains must entail intergranular interpenetration, as shown in Fig. 3. Grain interpenetration can only be avoided if the interpenetrating volumes could be accommodated by the creep deformation of grains. Local accommodation in the form of fold formation at triple lines [43] or sub-grain formation near grain boundaries [44] has been observed experimentally. In a three-dimensional microstructure, therefore, grain boundary sliding is necessarily creep-constrained [16, 17].

2.1.3. Brittle rupture condition The assumption that the idealized microstructure is comprised of indistinguishable grains yields a geometric rupture condition. An infinitely long macroscopic crack forms when any two facets of the rhombic dodecahedron sharing an edge, e.g., 1 and 5, or 1 and 9, but not 1 and 4 in Figure 1(a) or Figure 2 fail, i.e., become fully damaged. In the present work, we identify the formation of the macroscopic crack with rupture. For instance, suppose facets 1 and 5 fail. This implies the failure of facets $\vartheta_1 = 3$ and $\vartheta_5 = 11$ also in all the grains of the microstructure. The infinite crack can be traversed by repeatedly moving from facet 1 of one grain to facet 3 of

its neighboring grain through facet 5 of the first grain which overlaps facet 11 of the neighbor, and so on.

2.2. Creep deformation

2.2.1. Kinematics The evolution of the reference or undeformed state of the idealized polycrystal into the deformed state is treated using standard continuum mechanics described e.g., in Gurtin [45]. Grains are assumed to deform homogeneously with uniform deformation gradient \mathbf{F}^g . Assuming zero spin of a representative material point within a grain, which is appropriate to the symmetrical microstructure and loading shown in Fig. 1(a), \mathbf{F}^g evolves following

$$\dot{\mathbf{F}}^g = \dot{\boldsymbol{\epsilon}}^g \mathbf{F}^g, \quad (2)$$

where $\dot{\boldsymbol{\epsilon}}^g$ denotes the Eulerian rate of deformation of grains.

Because in addition to the processes underlying grain deformation, damage and grain boundary sliding processes also contribute to the macroscopic deformation, the macroscopic strain rate $\dot{\boldsymbol{\epsilon}}$ will generally differ from the grain strain-rate, $\dot{\boldsymbol{\epsilon}}^g$. The macroscopic shape will be characterized by the macroscopic deformation gradient \mathbf{F} , which, paralleling (2) evolves according to

$$\dot{\mathbf{F}} = \dot{\boldsymbol{\epsilon}} \mathbf{F}. \quad (3)$$

2.2.2. Ductile failure condition The eigenvalues of the stretch tensor, $\mathbf{U} = \sqrt{\mathbf{F}^T \mathbf{F}}$ are denoted λ_1 , λ_2 and λ_3 and ordered as $\lambda_1 \geq \lambda_2 \geq \lambda_3$. Following Hoff [46], ductile rupture is associated with $\lambda_1 \uparrow \infty$ and $\lambda_2 \lambda_3 \downarrow 0$.

Since it is not numerically possible to let $\lambda_1 \uparrow \infty$, the model microstructure is taken to have ruptured in a ductile manner when

$$\lambda_1 \geq C \lambda_3, \quad (4)$$

for sufficiently large C .

2.2.3. Loading and stresses Creep tests based on the widely used ASTM standard E-139 [47] are performed at constant load, i.e., at constant nominal stress. The nominal or Piola-Kirchhoff stress $\bar{\mathbf{S}}$ imposed macroscopically is related to the macroscopic Cauchy stress $\bar{\boldsymbol{\sigma}}$ through [45]

$$\bar{\mathbf{S}} = \det(\mathbf{F}) \bar{\boldsymbol{\sigma}} \mathbf{F}^{-T}, \quad (5)$$

where \mathbf{F} , introduced in Section 2.2.1 denotes the macroscopic deformation gradient. Because of the similarity of all grains in the idealized microstructure, the stress-distribution in all grains must be identical and therefore, the average stress in a grain must equal the macroscopic stress imposed upon the polycrystal. In the following analysis, for simplicity, we assume that stress is distributed uniformly in each grain.

If \mathbf{S}^g and $\boldsymbol{\sigma}^g$ are the uniform nominal and Cauchy stress in a grain, respectively, we then have

$$\mathbf{S}^g = \bar{\mathbf{S}}, \quad \text{and} \quad \boldsymbol{\sigma}^g = \bar{\boldsymbol{\sigma}} \quad (6)$$

in view of the indistinguishability of grains.

2.2.4. Creep constitutive law of grains Under a general state of stress, following Odqvist [48], we assume that each grain deforms by power-law Norton creep [49] according to

$$\dot{\boldsymbol{\epsilon}}^g = \frac{3}{2} \left(\frac{\sigma_e}{\sigma_c} \right)^{n-1} \frac{\mathbf{s}^g}{\sigma_c}, \quad (7)$$

where $\dot{\boldsymbol{\epsilon}}^g$ and \mathbf{s}^g denote the strain-rate and deviatoric Cauchy stress tensors in a grain, respectively, σ_c is a scalar stress reference, $\sigma_e = (3s_{ij}^g s_{ij}^g / 2)^{1/2}$ is the equivalent stress and n is the creep exponent.

Equation (7) describes the creep deformation of a grain. It makes no allowance for grain boundary sliding, which will be considered next.

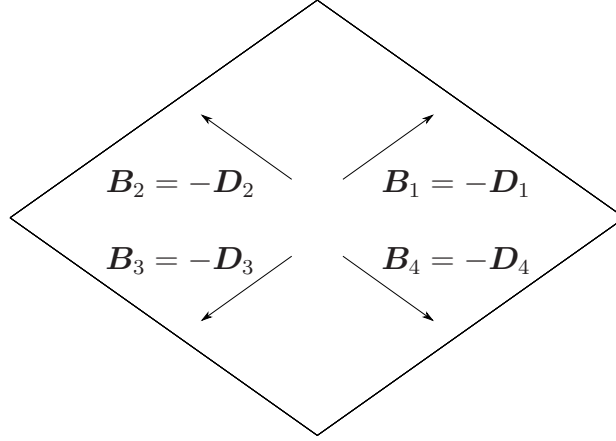


Figure 4. Sliding and cracking systems associated with a facet of the rhombic dodecahedron. Relative sliding between two neighboring grains in the present model can occur along one of four directions $\mathbf{B}_1, \dots, \mathbf{B}_4$ that are parallel to the edges of the common facet. $\mathbf{D}_1, \dots, \mathbf{D}_4$ are the assumed directions of propagation of wedge-cracks.

2.2.5. Grain-boundary sliding For simplicity and modeling convenience, rather than attempting to exactly capture the complex and somewhat incompletely understood

physical phenomena underlying grain boundary processes, grain boundary sliding is described in terms of four grain boundary sliding ‘systems’ associated with each facet f . The set of all sliding systems associated with facet f are denoted \mathcal{S}_f and the facet of sliding system s by f_s . Each sliding system $s \in \mathcal{S}_f$ is comprised of a sliding direction, \mathbf{B}_s , parallel to an edge of the facet f in the undeformed grain (Figure 4) and a sliding plane normal, \mathbf{N}_s , parallel to the facet normal, \mathbf{N}_f . \mathbf{B}_s and \mathbf{N}_s are unit vectors. These vectors map to the unit vectors

$$\begin{aligned}\mathbf{b}_s &= \mathbf{F}^g \mathbf{B}_s / \|\mathbf{F}^g \mathbf{B}_s\| \\ \mathbf{n}_s &= \mathbf{F}^{g-T} \mathbf{N}_s / \|\mathbf{F}^{g-T} \mathbf{N}_s\|\end{aligned}\quad (8)$$

in the deformed grain. It easily follows from (8) that $\mathbf{b}_s \cdot \mathbf{n}_s = \mathbf{B}_s \cdot \mathbf{N}_s = 0$. The sliding displacement in sliding system s is denoted by S_s . In order to obtain the evolution rate of S_s , it must be recognized that S_s evolves due to both grain deformation and grain boundary sliding. Denoting these separate contributions by \dot{S}_s^{def} and \dot{S}_s^{slid} , respectively, we have

$$\dot{S}_s = \dot{S}_s^{\text{def}} + \dot{S}_s^{\text{slid}}. \quad (9)$$

Standard continuum mechanics considerations [45] yield

$$\dot{S}_s^{\text{def}} = (\dot{\epsilon}^g \mathbf{b}_s \cdot \mathbf{b}_s) S_s. \quad (10)$$

To obtain \dot{S}_s^{slid} , the empirical constitutive law of Horton [39], which accounts for the effect of creep constraints (Section 2.1.2) on grain boundary sliding will be followed. Horton’s constitutive law decomposes the resolved shear stress in sliding system s , τ_s , defined as [50]

$$\tau_s = \max(0, \text{tr}(\boldsymbol{\sigma}^g \mathbf{n}_s \otimes \mathbf{b}_s)) \quad (11)$$

into two parts,

$$\tau_s = \tau_s^s + \tau_s^a. \quad (12)$$

τ_s^s and τ_s^a are considered to drive the basic grain boundary sliding process and the accommodation process at triple lines, respectively. This implies that $\tau_s^s \dot{S}_s^{\text{slid}}$ and $\tau_s^a \dot{S}_s^{\text{slid}}$ represent the power expended in grain boundary sliding and triple line accommodation, respectively. Using an approximation for the triple line stress concentration due to Zener [51], Horton’s [39] final expression written in the present notation is

$$\tau_s = T^s \left(\frac{\dot{S}_s^{\text{slid}}}{\dot{S}_0} \right)^{1/n_s} + T^a \left[\frac{1}{K_0} \left(\frac{\kappa_0}{\kappa} \right)^m \right] \left(\frac{\dot{S}_s^{\text{slid}}}{\dot{S}_0} \right)^{1/n_a}, \quad (13)$$

where \dot{S}_0 denotes a reference sliding rate, K_0 denotes the stress-concentration at triple lines due to sliding and κ_0 denotes a reference grain size. Reference stresses T^s and T^a determine the critical resolved shear stresses needed to overcome basic grain boundary sliding and accommodation processes, respectively. $T^s \ll T^a$ corresponds to free sliding grain boundaries, assumed in the analyses of Anderson and Rice [9]. The other limit, $T^a \ll T^s$, corresponds to unconstrained grain boundary sliding and is perhaps not physical in three dimensional microstructures [9].

Exponents n_s and n_a in (13) are associated with the basic grain boundary sliding process and the accommodation process, respectively. It is well-established [52] that grain boundary sliding is caused by the motion of grain boundary dislocations. Many experimental bicrystal studies [53, 52] and theoretical models [54, 55] suggest that $n_s = 1$ for pure grain boundary sliding and $n_s = 2$ for stimulated grain boundary sliding in pure metals. In austenitic stainless steels, however, carbide precipitates form at grain boundaries during creep deformation, which may lead to $n_s > 2$ [56]. On the other hand, since the accommodation process is power-law creep driven, $n_a = n$, the Norton exponent of (7).

In addition to Norton creep within grains (7), grain boundary sliding also contributes to the macroscopic strain-rate, $\dot{\epsilon}^g$. The latter contribution can be estimated by approximating grain boundary sliding as a simple shear deformation smeared over the entire grain with shearing rate,

$$\dot{\gamma}_s = \dot{S}_s^{\text{slid}} / \kappa, \quad (14)$$

with shear direction \mathbf{b}_s and shear plane normal \mathbf{n}_s . Such deformation is familiar from crystallographic slip. Crystal plasticity theory [50] then gives the contribution of grain boundary sliding to the overall rate of deformation as $\sum_s \dot{\gamma}_s \mathbf{m}_s$, where

$$\mathbf{m}_s = (\mathbf{b}_s \otimes \mathbf{n}_s + \mathbf{n}_s \otimes \mathbf{b}_s) / 2, \quad (15)$$

denotes the Schmid tensor of sliding system s . The effect of smearing out localized grain boundary sliding over the entire domain of the grain is that whereas grain boundary sliding entails specimen volume increase, the strain-rate obtained by smearing grain boundary sliding \dot{S}_s^{slid} into a homogeneous bulk shear, $\sum_s \dot{\gamma}_s \mathbf{m}_s$, is volume conserving. Superposing the strain-rate due to grain boundary sliding on all sliding systems $s \in \cup_{f=1}^{12} \mathcal{S}_f$ with that due to creep deformation of the grain, given by (7), we obtain

$$\dot{\epsilon} = \dot{\epsilon}^g + \sum_{f=1}^{12} \sum_{s \in \mathcal{S}_f} \dot{\gamma}_s \mathbf{m}_s. \quad (16)$$

2.3. Damage micromechanisms

2.3.1. Wedge cracking Wedge-cracks are known to form in AISI type 304 and 316 austenitic stainless steels by the rapid growth and coalescence of cavities (w-type voids) near triple lines [24, 37, 23, 25] in the intermediate stress regime [22]. The rapid growth of such cavities is attributed to tensile stress concentration near the triple lines [24].

The present model for wedge cracking is derived from the models of Cottrell [1] and Williams [2]. Cottrell [1] treated the opening displacement induced by sliding grain boundaries, S_1, S_2 and S_3, S_4 in Figure 5, as a pair of hollow dislocations. Free energy considerations then yield the stable wedge crack length. Using an estimate of the sliding rate of grain boundaries in terms of the minimum creep rate, Williams [2] obtained the time to rupture of a grain boundary facet, which he regarded as a conservative estimate of the time to macroscopic rupture. Although neither model explicitly accounts for the

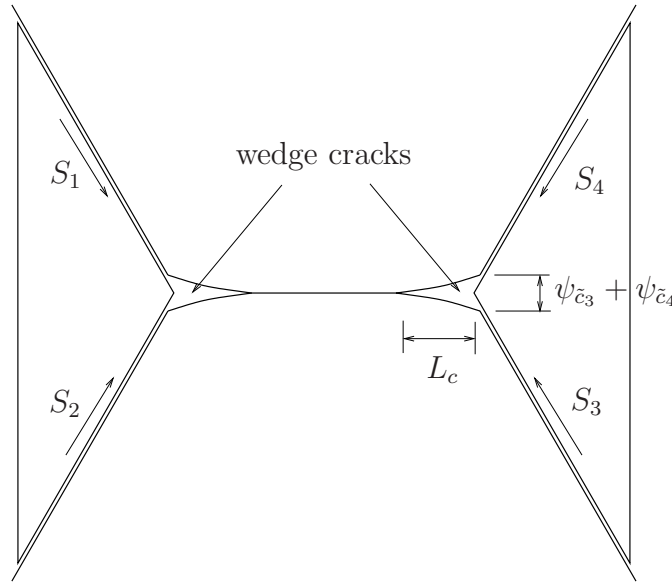


Figure 5. Cracking along a grain boundary facet is induced by grain boundary sliding. Shown here is a type (b) crack in the classification of Chang and Grant [19].

diffusion-assisted cavity growth mechanism for the extension of wedge-cracks, diffusion effects are approximately considered in terms of an effective free surface energy, Γ , associated with forming new wedge-crack surfaces.

In the present model, sliding can occur in any of 48 sliding systems on the 12 facets of the rhombic dodecahedral grain. In parallel with the structure of the sliding systems, four cracking systems are associated with each facet f . The set of all cracking systems associated with facet f are denoted by \mathcal{C}_f and the facet containing cracking system c by f_c . Each cracking system $c \in \mathcal{C}_f$ is comprised of a crack propagation direction, \mathbf{D}_c in the reference configuration, chosen in the opposite sense of the corresponding sliding direction shown in Figure 4. As with \mathbf{B}_s in (8), \mathbf{D}_c evolves with the shape of the grain to $\mathbf{d}_c = \mathbf{F}^g \mathbf{D}_c / \|\mathbf{F}^g \mathbf{D}_c\|$ in the deformed configuration. We also assign a normal to cracking system c in the reference configuration \mathbf{N}_c that is parallel to the facet normal and evolve it with deformation according to $\mathbf{n}_c = \mathbf{F}^{g-T} \mathbf{N}_c / \|\mathbf{F}^{g-T} \mathbf{N}_c\|$ as in (8). Wedge cracks are assumed to open in pure mode I with the opening displacement parallel to \mathbf{N}_c .

Figure 5 schematically shows two wedge-cracks formed in a grain boundary. S_i , $i = 1, \dots, 4$ denote sliding displacements in the sliding systems that cause the wedge-cracks. For $S_1 > 0$, $S_2 > 0$, $S_3 > 0$ and $S_4 > 0$, as shown in Figure 5, two type (b) wedge-cracks in the nomenclature of Chang and Grant [19] form. The structure of the cracking systems assumed above, however, can represent all three Chang-Grant wedge-cracking modes. Thus, if $S_1 = S_4 = 0$ and $S_2 > 0$, $S_3 > 0$, or if $S_2 = S_3 = 0$ and $S_1 > 0$, $S_4 > 0$, we would have two type (a) wedge-cracks in Figure 5. Finally, if the directions of all sliding motions were reversed, we would obtain two type (c) cracks in the Chang-Grant nomenclature.

As shown in Figure 5, an active sliding system $s \in \mathcal{S}_f$ on facet f with $\dot{S}_s > 0$ can activate a cracking system $c \in \mathcal{C}_{f_1}$ in one of the neighboring facets, $f_1 \in \mathcal{N}_f$. The geometry of the rhombic dodecahedron and that of the sliding and cracking systems associated with it enable us to uniquely identify the cracking system \tilde{c}_s activated by sliding system $s \in \mathcal{S}_f$ as

$$\tilde{c}_s = \{c \in \mathcal{C}_{f_1} : f_1 \in \mathcal{N}_{f_s}, \mathbf{B}_s \cdot \mathbf{N}_c > 0\}. \quad (17)$$

Furthermore, we denote the crack opening displacement in cracking system \tilde{c}_s caused by sliding displacement S_s by $\psi_{\tilde{c}_s}$ and define

$$\psi_{\tilde{c}_s} = S_s \mathbf{b}_s \cdot \mathbf{n}_{\tilde{c}_s}. \quad (18)$$

For later use, we also associate each cracking system c in facet f , $c \in \mathcal{C}_f$ with a cracking system ϑ_c on the opposite facet ϑ_f , i.e., $\vartheta_c \in \mathcal{C}_{\vartheta_f}$ such that $\mathbf{D}_c = \mathbf{D}_{\vartheta_c}$. Thus, cracking systems c and ϑ_c are associated with essentially the same wedge-crack in the periodic microstructure. In Figure 5, cracking systems \tilde{c}_1 and \tilde{c}_2 are opposites of each other, i.e., $\vartheta_{\tilde{c}_1} = \tilde{c}_2$. Similarly, $\vartheta_{\tilde{c}_3} = \tilde{c}_4$. As shown, $\psi_c + \psi_{\vartheta_c}$ gives the total wedge-crack opening displacement.

2.3.2. Cavitation In addition to wedge cracks formed by coalescence of rapidly growing voids near triple lines, cavities (r-type voids) are observed to develop on grain boundary facets [24, 25, 57, 58] away from triple lines, particularly in areas with a concentration of carbide particles. Cavity shape and growth rate depend on the dislocation structure of the grain boundary, presence of particles at the grain boundary and the grain boundary sliding rate.

Cavities in the present model are associated with sliding systems, $s \in \cup_{f=1}^{12} \mathcal{S}_f$. Although they are known to nucleate throughout the creep process and grow into either a spherical shape or a crack-like shape depending on the relative rates of diffusional and grain boundary sliding processes, in the present model, following Evans [3, 22], cavity nuclei are idealized to form at the outset with density N per unit grain boundary surface area and develop into cuboidal cavities of constant width w and height h . Cavity growth can thus occur only by extending the cavity length l_s along the sliding direction \mathbf{b}_s . Following Evans [3], it is also assumed that $w \ll l_s$ and $h \ll l_s$. The effective cavity surface energy is denoted by γ . Because they are smaller and more numerous than wedge-cracks, cavities are assumed not to induce a stress-intensity, unlike wedge-cracks [22, Section 3.2.2]. The load dropped by the cavitated area in a facet is assumed to uniformly overload the uncavitated area of that facet.

As noted in Section 1 cavity extension in the present model can occur either by a mechanism of diffusion or by a mechanism of deformation. Cavity extension rates obtained assuming the former mechanism are denoted \dot{l}_s^D and those obtained assuming the latter are denoted \dot{l}_s^E .

In the absence of grain boundary sliding, cavities grow by a mechanism of diffusion and creep. A well-developed theory for cavity growth that accounts for diffusive and creep contributions in an unconstrained facet is available [6, 7, 10, 12]. By idealizing

a cavitated facet as a bridged crack, Rice [17] has obtained constrained cavity growth rates when cavitated facets are widely separated. Cocks and Ashby [8] and Anderson and Rice [9] have considered the case of interacting facets. In this work, we assume that diffusion dominates creep as the mechanism for constrained cavity growth and follow the treatment of Cocks and Ashby [8] to obtain cavity growth rates. Letting F_f denote the cavitated area fraction of a grain boundary facet f , they obtain

$$\dot{F}_f = -\frac{\Phi_1}{\sqrt{F_f} \log F_f} \sigma_f^{\text{cav}}, \quad (19)$$

where, σ_f^{cav} , the normal stress experienced by the cavity is determined by the creep constraints [8],

$$F_f = \sum_{s \in \mathcal{S}_f} N w l_s, \quad (20)$$

and

$$\Phi_1 = \frac{8 D_B \delta_B \Omega}{3 k T \ell^3}. \quad (21)$$

Here, D_B is the grain boundary diffusion coefficient, δ_B is the grain boundary thickness, Ω is the atomic volume, k is the Boltzmann constant, T is the absolute temperature, and ℓ is half the intercavity spacing.

Using considerations of load sharing between the cavitating facet and the bulk of the neighboring grains, Cocks and Ashby [8] have derived an expression for σ_f^{cav} in (19) according to which, $\sigma_f^{\text{cav}} \leq \sigma_s = \boldsymbol{\sigma}^g \mathbf{n}_s \cdot \mathbf{n}_s$, the resolved normal traction on facet f , for $s \in \mathcal{S}_f$. The limiting case $\sigma_f^{\text{cav}} = \sigma_s$ for $s \in \mathcal{S}_f$ corresponds to cavity growth by a mechanism of unconstrained diffusion. In the present work, for simplicity, we assume that $\sigma_f^{\text{cav}} = \sigma_s$ for $s \in \mathcal{S}_f$. This assumption is conservative as it overestimates the cavity growth rate.

The growth rate of a cavity by a diffusional mechanism is denoted \dot{l}_s^{D} . On a grain boundary devoid of sliding, according to (20),

$$\dot{F}_f = N w \sum_{s \in \mathcal{S}_f} \dot{l}_s^{\text{D}}. \quad (22)$$

Now, since the normal stress experienced by a cavity on grain boundary facet f , σ_f^{cav} , is independent of s , the diffusional extension rate of cavities associated with all four sliding systems must be identical. Thus, $\dot{F}_f = 4 N w \dot{l}_s^{\text{D}}$ if $s \in \mathcal{S}_f$. Combining this with (19), we have

$$N w \dot{l}_s^{\text{D}} = -\frac{\Phi_1/4}{\sqrt{\sum_{s \in \mathcal{S}_f} N w l_s} \log(\sum_{s \in \mathcal{S}_f} N w l_s)} \sigma_s \quad (23)$$

for the rate of cavity extension by a mechanism of diffusion on a grain boundary facet devoid of sliding.

The foregoing considerations do not apply when significant grain boundary sliding also occurs on the cavitating facet. A mechanistically rigorous model for diffusion assisted cavity growth in a sliding grain boundary is due to Chen [26]. By balancing

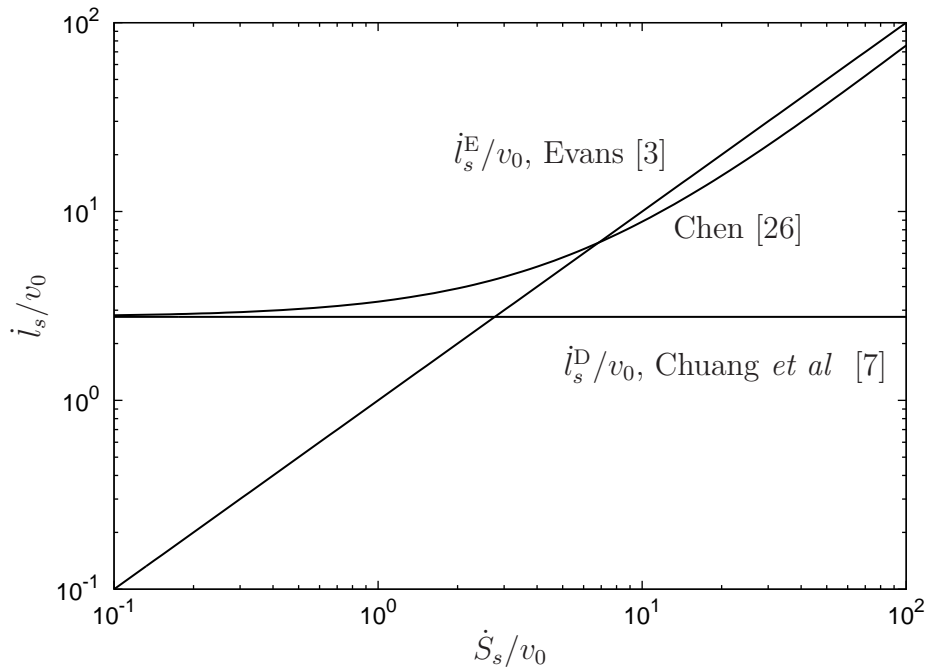


Figure 6. Rate of cavitation predicted on a sliding grain boundary facet by Chen [26] compared with that predicted by Evans [22], \dot{l}_s^E and that predicted by Chuang [7], \dot{l}_s^D by unconstrained diffusion in the absence of grain boundary sliding.

the atomic flux at the tip of a non-equilibrium crack-like cavity, Chen [26] derived the relation between the normalized grain boundary sliding rate \dot{S}_s/v_0 and the normalized cavity extension rate \dot{l}_s/v_0 as

$$2 \sin(\psi/2) \left(\frac{\dot{l}_s}{v_0} \right)^{\frac{2}{3}} + \tan(\psi/2) \left(\frac{\dot{l}_s - \dot{S}_s}{v_0} \right) = \frac{3}{M} \left[\tilde{\Sigma} - 2 \sin(\psi/2) \left(\frac{\dot{l}_s}{v_0} \right)^{\frac{1}{3}} \right]. \quad (24)$$

Here v_0 is a reference speed, $\tilde{\Sigma}$ is the normalized applied stress and M contains diffusion constants and geometric factors. ψ denotes the dihedral angle between the two intersecting surfaces at the cavity tip. We refer to Chen [26] for the derivation of (24) and the normalization scheme. Equation (24) is an implicit equation for \dot{l}_s/v_0 in terms of \dot{S}_s/v_0 . Fig. 6 shows the dependence of \dot{l}_s/v_0 on \dot{S}_s/v_0 for typical values of the various parameters used by Chen [26, Fig. 3]: $\psi = 80^\circ$, $\tilde{\Sigma} = 10$ and $M = 5$. It is seen that for grain boundary sliding speeds that satisfy, $\dot{S}_s/v_0 \geq 10$, Chen's model predicts that $\dot{S}_s \approx \dot{l}_s$. For small \dot{S}_s , however, Chen's model asymptotes to the cavity growth rate of Chuang and Rice [6] and Chuang *et al* [7] in the absence of grain boundary sliding. As noted in Section 1, however, Chen's model requires further development to obtain the cavity opening rate and to include the effects of localized grain creep and constraints.

Evans [3, 22] has treated cavity growth on sliding grain boundaries on the basis of quite different considerations. Evans' model does not explicitly represent diffusional processes. Rather, by balancing the free energy changes that accompany cavity

extension, i.e., added surface energy, reduced strain energy and reduced potential energy of the loading mechanism, it predicts a cavity extension rate, \dot{l}_s^E . Diffusional processes, in Evans' model [3, 22], are treated as complex microscopic processes whose role is represented by suitably augmenting the cavity surface energy, γ . Such treatment of complex microscopic mechanisms is familiar in the fracture mechanics of all but ideally brittle materials.

For steady state cavitation during grain boundary sliding, as seen from Fig. 6, Evans' model [3, 22] predicts $\dot{l}_s^E = \dot{S}_s$ and thus agrees with Chen's model in the intermediate stress range $\dot{S}_s/v_0 \geq 10$. For small \dot{S}_s , however, the two models diverge and Chen's model predicts a much higher rate of cavity growth. Physically, this is because Evans' model only applies when cavity growth is controlled solely by grain boundary sliding whereas, Chen's model correctly recognizes that even without any grain boundary sliding, $\dot{S}_s = 0$, cavity growth can proceed by diffusional mechanisms alone at non-zero rate, \dot{l}_s^D . In the present work, we therefore take cavity growth to follow

$$\dot{l}_s = \max(\dot{l}_s^E, \dot{l}_s^D). \quad (25)$$

As seen from Fig. 6, this suffices to bring both models into reasonable coincidence over both low and intermediate grain boundary sliding rates. Although Chen's model [26] is more mechanistically rigorous, we follow Evans' model with the correction given by (25) in the present work as it is more amenable for incorporation into the energy argument to be developed in Section 2.4 below.

2.4. Energy considerations and damage evolution

The damage variables in the present model are the wedge-crack lengths $L_c \geq 0$, associated with the various cracking systems, $c \in \cup_{f=1}^{12} \mathcal{C}_f$ and cavity lengths $l_s \geq 0$ associated with the various sliding systems $s \in \cup_{f=1}^{12} \mathcal{S}_f$. L_c and l_s are defined in the current or deformed configuration. For later use, we also define quantities L_c^* and l_s^* representing the pull-back of L_c and l_s to the reference configuration as [59]

$$L_c^* = L_c \|\mathbf{F}^{g-1} \mathbf{b}_c\|, \quad \text{and} \quad (26)$$

$$l_s^* = l_s \|\mathbf{F}^{g-1} \mathbf{b}_s\|. \quad (27)$$

The approach taken below to obtain evolution equations for these damage variables extends and unifies the analyses of Williams [2, 60] for wedge-crack growth and Evans [3, 22] for cavitation due to grain boundary sliding by (i) coupling the cavitation and wedge-cracking modes of damage accumulation, (ii) simultaneously treating the damage evolution processes occurring on all facets of the grain, (iii) including a treatment of accommodation processes that must necessarily accompany grain boundary sliding as discussed in Section 2.2.5 and (iv) allowing for grain deformation during damage evolution.

The expression for the change in free energy, ΔG associated with the damage variables changing from 0 to L_c for each cracking system $c \in \cup_{f=1}^{12} \mathcal{C}_f$ and from 0 to l_s for each sliding system $s \in \cup_{f=1}^{12} \mathcal{S}_f$ are derived subject to two restrictions. First, damage

evolution is effected keeping the grain shape, \mathbf{F}^g , fixed in the current configuration, thereby physically decoupling the homogeneous grain deformation processes from the damage processes at the grain boundaries. Grain deformation near triple lines that accommodate grain boundary sliding as explained in Section 2.2.5 is, however, treated as a grain boundary process that evolves during the virtual damage evolution. Second, cavitation is assumed to occur due to grain boundary sliding. In the notation of Sec. 2.3.2, cavity lengths given by this calculation correspond to l_s^E and not l_s^D . Correction terms that serve to relax these restrictions will be derived at the end of this section.

The change in free energy of a grain in going from the undamaged state to a damaged state is obtained by summing over the change in free energy associated with each of its sliding and cracking modes:

$$\Delta G = \sum_{f=1}^{12} \left[\sum_{s \in \mathcal{S}_f} \Delta G_s + \sum_{c \in \mathcal{C}_f} \Delta G_c \right]. \quad (28)$$

Strain-energy contributions to the free-energy depend on elastic properties of the grains. We assume the grains to have Hookean elastic properties with Young's modulus E , Poisson's ratio ν and shear modulus $\mu = E/(2(1 + \nu))$.

ΔG_s in (28) in going from $l_s^E = 0$ to the damaged state $l_s^E \geq 0$ is given by

$$\Delta G_s = \frac{\kappa_1^2}{2} \left[Nw \left(2\gamma l_s^E - \sigma_s h l_s^E - \frac{\sigma_s^2}{E} l_s^E h \right) - \tau_s^s S_s \right]. \quad (29)$$

Here, $\sigma_s = \boldsymbol{\sigma}^g \mathbf{n}_s \cdot \mathbf{n}_s$ is the normal traction acting on the sliding system s and γ is the surface energy per unit area associated with cavity formation. The term $2\kappa_1^2 Nw\gamma l_s^E$ on the right side of (29) corresponds to the increase in surface energy, the term $-\kappa_1^2 Nw\sigma_s h l_s^E$ corresponds to the decrease in the potential energy due to lowering of the loading point and the term $-\kappa_1^2 Nw\sigma_s^2 l_s^E h/E$ corresponds to the decrease in elastic strain energy if the stress dropped by the cavitated area on a grain boundary is assumed uniformly distributed over the uncavitated area, all due to cavity formation. $-\tau_s^s S_s$ is the work done on the grain by the external loading agency to effect sliding through distance S_s . Internally, this energy will be partially dissipated in the course of grain boundary dislocation motion and partially utilized to cause grain boundary ledge motion for cavity growth [3, 52]. Since two grains meet at the facet containing sliding system s , the change in free energy per grain is only half the term in square brackets in the right side of (29). The part of the work done by the external loading agency, $-\tau_s^a S_s$ to overcome the geometric constraint to sliding in the idealized microstructure described in Secs. 2.1 and 2.2.5 is not available to the cavitation process, as it is dissipated in the course of the accommodative deformation processes near the triple lines in the grain. It is therefore not included in the expression of (29).

If τ_s^s were replaced by τ_s in (29), the free energy expression given there would coincide with that of Evans [22]. Evans[3, 22] thus regarded the work of accommodation at triple lines as part of the surface energy of a cavity and obtained values of the surface

energy two or three orders of magnitude larger than reasonable. He attributed the excess surface energy to the inelastic processes that must accompany grain boundary sliding and cavity growth. Removal of the energy corresponding to constraint accommodation in (29), as done presently, should reduce the overestimation of the effective surface energy. However, even in the present form, the surface energy will be overestimated, as it must account for the diffusional and creep processes accompanying cavity extension in ductile materials.

Prior to obtaining the expression for the change in free energy of a cracking system, we define the total damage in facet f ,

$$\phi_f = \left(\sum_{s \in \mathcal{S}_f} \kappa_1^2 N w l_s^* + \sum_{s \in \mathcal{C}_f} \kappa_1 L_c^* \right) / \kappa_1^2. \quad (30)$$

The two terms in the numerator of (30) are the facet areas in the reference configuration covered by cavities and wedge-cracks, respectively. Overgrowth of a cavity by a wedge-crack, overgrowth of cavities of multiple sliding systems or overgrowth of cracks from multiple cracking systems on the same facet has been neglected. Also, the area of the facet $\sqrt{2}\kappa^2$ has been approximated by $\kappa_1^2 = 1.5\kappa^2$, which constitutes the denominator of (30). In terms of ϕ_f , the change in free energy of cracking system c in going from $L_c = 0$ to $L_c > 0$ is

$$\begin{aligned} \Delta G_c = \frac{1}{2} \left[\frac{\mu \kappa_1}{4\pi(1-\nu)} (\psi_c + \psi_{\vartheta_c})^2 \ln \left(\frac{4R}{L_c} \right) 1_{[\phi_{fc} < 1]} + 2\kappa_1 \Gamma L_c \right. \\ \left. - \kappa_1 \frac{\pi K_c (1-\nu) \sigma_c^2}{4\mu} L_c^2 - \kappa_1 \frac{\sigma_c (\psi_c + \psi_{\vartheta_c})}{2} L_c \right]. \end{aligned} \quad (31)$$

This equation is a modification of one due to Cottrell [1]. The first term represents the energy of a hollow dislocation of Burgers vector length $\psi_c + \psi_{\vartheta_c}$. Physically, the hollow dislocation is created by grain boundary sliding. R denotes a cut-off length at which the integration to obtain the dislocation strain-energy is stopped. Evans [22, Section 6.3.2] has argued that the energy contribution from the hollow dislocation must be included only if the facet f_c resists grain boundary sliding. Thus, the first term is to be included only if the facet of cracking c itself is not completely damaged ($\phi_{fc} < 1$). The second term in the right side of (31) is the effective surface energy of the crack. The third term is the change in elastic energy caused by wedge-cracking. Since by the geometry of the microstructure, cracks form in a periodic pattern, stress fields of different wedge-cracks may interact. K_c is a parameter in the third term to account for this interaction. With $K_c = 1$, the third term represents the reduction in strain-energy caused by extension to length L_c of an interaction-free crack. Finally, the fourth term is the loss of potential energy of the loading mechanism due to crack opening. As noted in connection with (29) for the effective surface energy γ , Γ in (31) too includes not only the true surface energy of the grain boundary material, but also the energy dissipated in the inelastic processes that accompany crack extension.

Normalizing length-like quantities as

$$\begin{aligned}
\hat{l}_s &= Nw l_s, \\
\hat{l}_s^* &= Nw l_s^*, \\
\hat{l}^E &= Nw \hat{l}^E, \\
\hat{h} &= h/\kappa_1, \\
\hat{S}_s &= S_s/\kappa_1, \\
\hat{\psi}_c &= \psi_c/\kappa_1, \\
\hat{L}_c &= L_c/\kappa_1, \\
\hat{L}_c^* &= L_c^*/\kappa_1, \\
\hat{r}_c &= 4R/\kappa_1,
\end{aligned} \tag{32}$$

stress-like quantities as

$$\begin{aligned}
\hat{\tau}_s^s &= \tau_s^s \kappa_1 / \gamma, \\
\hat{\sigma}_c &= \sigma_c \kappa_1 / \gamma, \\
\hat{\sigma}_s &= \sigma_s \kappa_1 / \gamma,
\end{aligned} \tag{33}$$

elastic moduli as

$$\begin{aligned}
\hat{E} &= E \kappa_1 / \gamma, \\
\hat{\mu} &= \mu \kappa_1 / (8\pi(1 - \nu)\gamma),
\end{aligned} \tag{34}$$

and the effective surface energy associated with cracking systems as

$$\hat{\Gamma} = \Gamma / \gamma, \tag{35}$$

we obtain the normalized free energy change associated with sliding system s , $\Delta \hat{G}_s = \Delta G_s / (\kappa_1^2 \gamma)$ as

$$\Delta \hat{G}_s = \hat{l}_s \left(1 - \frac{\hat{\sigma}_s \hat{h}}{2} - \frac{\hat{\sigma}_s^2 \hat{h}}{2\hat{E}} \right) - \frac{\hat{\tau}_s^s \hat{S}_s}{2} \tag{36}$$

and the normalized free energy associated with cracking system c , $\Delta \hat{G}_c = \Delta G_c / (\kappa_1^2 \gamma)$ as

$$\Delta \hat{G}_c = \hat{\mu} (\hat{\psi}_c + \hat{\psi}_{\vartheta_c})^2 \ln \left(\frac{\hat{r}}{\hat{L}_c} \right) 1_{[\phi_{fc} < 1]} + \hat{\Gamma} \hat{L}_c - \frac{\hat{\sigma}_c^2 K_c}{64\hat{\mu}} \hat{L}_c^2 - \frac{\hat{\sigma}_c (\hat{\psi}_c + \hat{\psi}_{\vartheta_c})}{4} \hat{L}_c. \tag{37}$$

Further, in terms of the normalized variables, the damage associated with facet f , given by (30), takes the simple form

$$\phi_f = \sum_{s \in \mathcal{S}_f} \hat{l}_s^* + \sum_{c \in \mathcal{C}_f} \hat{L}_c^*. \tag{38}$$

Also, in terms of the normalized free-energies associated with the sliding and cracking systems, we may write the total free energy change from the undamaged to the damaged state, given by (28) as

$$\Delta \hat{G} = \frac{\Delta G}{\kappa_1^2 \gamma} = \sum_{f=1}^{12} \left(\sum_{s \in \mathcal{S}_f} \Delta \hat{G}_s + \sum_{c \in \mathcal{C}_f} \Delta \hat{G}_c \right). \tag{39}$$

Steady-state damage evolution requires that

$$\left(\frac{\partial \Delta \hat{G}}{\partial \hat{L}_c} \right) = 0, \text{ for all } c \in \cup_{f=1}^{12} \mathcal{C}_f \text{ and} \quad (40)$$

$$\left(\frac{\partial \Delta \hat{G}}{\partial \hat{l}_s} \right) = 0, \text{ for all } s \in \cup_{f=1}^{12} \mathcal{S}_f. \quad (41)$$

In performing the partial differentiation of (40) all damage variables of the model, except L_c are kept fixed. Upon substituting the preceding equations in (40) we obtain

$$\left(\frac{\partial \Delta \hat{G}}{\partial \hat{L}_c} \right) = \left(\hat{\Gamma} - \frac{\hat{\sigma}_c}{4} (\hat{\psi}_c + \hat{\psi}_{\vartheta_c}) \right) - \hat{L}_c \left(\frac{\hat{\sigma}_c^2 K_c}{32 \hat{\mu}} \right) - 1_{[\phi_f < 1]} \frac{\hat{\mu}}{\hat{L}_c} (\hat{\psi}_c + \hat{\psi}_{\vartheta_c})^2 = 0, \quad (42)$$

which results in a linear or quadratic equation

$$\hat{L}_c^2 \left(\frac{\hat{\sigma}_c^2 K_c}{32 \hat{\mu}} \right) - \hat{L}_c \left(\hat{\Gamma} - \frac{\hat{\sigma}_c}{4} (\hat{\psi}_c + \hat{\psi}_{\vartheta_c}) \right) + 1_{[\phi_f < 1]} \hat{\mu} (\hat{\psi}_c + \hat{\psi}_{\vartheta_c})^2 = 0, \quad (43)$$

according as $\phi_{f_c} = 1$, or $\phi_{f_c} < 1$. For fixed crack-opening displacements ψ_c (43) determines the crack length L_c . In performing the partial differentiation of (41) all damage variables excepting \hat{l}_s^E are fixed. Accounting for the dependence of \hat{l}_s^E on \hat{S}_s [3], (41) yields

$$\begin{aligned} \left(\frac{\partial \Delta \hat{G}}{\partial \hat{l}_s^E} \right) &= \left(1 - \frac{\hat{\sigma}_s \hat{h}}{2} - \frac{\hat{\sigma}_s^2 \hat{h}}{2 \hat{E}} \right) - \left(\frac{\partial \hat{S}_s}{\partial \hat{l}_s^E} \right) \times \\ &\quad \left\{ \frac{\hat{\tau}_s}{2} - (\mathbf{b}_s \cdot \mathbf{n}_{\tilde{c}_s}) \left[1_{[\phi_{f_{\tilde{c}_s}} < 1]} 2 \hat{\mu} (\hat{\psi}_{\tilde{c}_s} + \hat{\psi}_{\vartheta_{\tilde{c}_s}}) \ln \left(\frac{\hat{r}}{\hat{L}_{\tilde{c}_s}} \right) - \frac{\hat{\sigma}_{\tilde{c}_s}}{4} \hat{L}_{\tilde{c}_s} \right] \right\} \\ &= 0. \end{aligned} \quad (44)$$

Since $\dot{\hat{l}}_s^E = (\partial \hat{l}_s^E / \partial \hat{S}_s) \dot{\hat{S}}_s$, this implies

$$\dot{\hat{l}}_s^E = \frac{\dot{\hat{S}}_s \left[\frac{\hat{\tau}_s}{2} - (\mathbf{b}_s \cdot \mathbf{n}_{\tilde{c}_s}) \left\{ 1_{[\phi_{\tilde{c}_s} < 1]} 2 \hat{\mu} (\hat{\psi}_{\tilde{c}_s} + \hat{\psi}_{\vartheta_{\tilde{c}_s}}) \ln \left(\frac{\hat{r}}{\hat{L}_{\tilde{c}_s}} \right) - \frac{\hat{\sigma}_{\tilde{c}_s}}{4} \hat{L}_{\tilde{c}_s} \right\} \right]}{\left(1 - \frac{\hat{\sigma}_s \hat{h}}{2} - \frac{\hat{\sigma}_s^2 \hat{h}}{2 \hat{E}} \right)}. \quad (45)$$

Equation (45) gives the cavity extension rate assuming the grain shape is frozen and that cavity growth is caused by grain boundary sliding. As noted in Section 2.3.2, at low grain boundary sliding speeds, cavity growth can proceed by a purely diffusional mechanism at the rate \dot{l}_s^D . It is assumed that wedge cracking does not accompany diffusional cavitation in the absence of significant grain boundary sliding. Thus, \dot{l}_s^D is taken to evolve uncoupled with L_c following (23), which, in terms of normalized variables,

$$\begin{aligned} \hat{l}_s^D &= N w l_s^D, \\ \hat{\Phi} &= \Phi \gamma / 4 \kappa_1, \end{aligned} \quad (46)$$

can be written as

$$\dot{\hat{l}}_s^D = - \frac{\hat{\Phi}_1}{\sqrt{\sum_{s \in \mathcal{S}_f} \hat{l}_s} \log(\sum_{s \in \mathcal{S}_f} \hat{l}_s)} \hat{\sigma}_s. \quad (47)$$

The normalized cavitation rate then follows from (25) as

$$\dot{\hat{l}}_s = \max(\dot{l}_s^D, \dot{l}_s^E). \quad (48)$$

As stated at the outset of the present Section 2.4, the foregoing expression was obtained by freezing the evolution of grain deformation \mathbf{F}^g . Freezing the damage processes described above and letting the cavity length l_s^E vary only with the grain deformation, we find from standard continuum mechanics that $\dot{\hat{l}}_s = (\dot{\epsilon}^g \mathbf{b}_s \cdot \mathbf{b}_s) \hat{l}_s$. Superposing these two rates, we find that the nett rate of cavity elongation is

$$\dot{\hat{l}}_s = (\dot{\epsilon}^g \mathbf{b}_s \cdot \mathbf{b}_s) \hat{l}_s + \max(\dot{l}_s^D, \dot{l}_s^E). \quad (49)$$

2.5. Simulation of creep damage evolution and rupture

Time integration of the grain boundary sliding and damage equations, (13), (49) and (43) until either the brittle rupture condition of Section 2.1.3 or the ductile rupture condition of Section 2.2.2 is satisfied gives the entire creep damage history and time to rupture. Over some parts of the creep deformation history, the evolution equations are stiff. In the present implementation, a standard subroutine suitable for stiff equations, `lsode` [61], was used with an analytically calculated Jacobian of the evolution equations.

3. Results and discussion

We now discuss the results obtained from simulating creep damage evolution leading up to creep rupture. Uniaxial creep-rupture tests following ASTM standard E-139 [47] are conducted at constant load. Accordingly, the simulation specimen is subjected to constant imposed nominal stress following

$$\bar{\mathbf{S}} = \Sigma_a \mathbf{N}_1 \otimes \mathbf{N}_1 = \Sigma_a \mathbf{N}_3 \otimes \mathbf{N}_3. \quad (50)$$

Here, the tensile axis is normal to facets 1 and 3 of the rhombic dodecahedral grain oriented as shown in Figure 1(a). We compare the time to rupture and failure mode in these simulations with the experimental observations of Mathew *et al* [34] and Sasikala *et al* [35].

Material parameters used for obtaining the present model predictions are listed in Table 1. A number of model variables, e.g., N and w of (22), do not appear in this table because they are normalized away in (32) and (46). Five of the listed values are fitting parameters; others are taken from the literature. Two of the fitting parameters, γ and Γ are the surface energies of cavities and cracks, respectively. The model predictions are insensitive to these in that variations upto 10% in these parameters do not alter the predicted lifetime appreciably. On the other hand, two other fitting parameters, T^s and T^a , determine the rate of constrained grain boundary sliding. The model prediction sensitively depends on them. Φ_1 determines cavity growth purely by constrained diffusion. The model predictions are significantly sensitive to Φ_1 at low stresses where the damage mechanism is diffusion dominated.

Parameter	Reference	Value
κ	(1); [34, 35]	35 μm
C	(4); numerical considerations	2
σ_c	(7); [34]	166 MPa
n	(7); [34]	11
\dot{S}_0	(13); arbitrary	10^{-9} s^{-1}
n_s	(13); [39]	3.3
n_a	(13); [39]	11
T^s	(13); fitting parameter	50 MPa
T^a	(13); fitting parameter	27 MPa
Φ_1	(21); fitting parameter	$6 \times 10^{-17} \text{ Pa}^{-1}$
γ	(29); fitting parameter	150 Jm^{-2}
R	(31);[22]	20 μm
E	(31); standard value	200 GPa
ν	(31); standard value	0.3
Γ	(31); fitting parameter	200 Jm^{-2}

Table 1. Material constants used to fit the time to rupture of the nuclear grade AISI type 316 steel of [34, 35]. Five of the listed values are fitting parameters; others are taken from the literature. Two of those, γ and Γ are the surface energies of cavities and cracks, respectively. The other two fitting parameters, T^s and T^a determine the rate of constrained grain boundary sliding. Φ_1 determines cavity growth purely by constrained diffusion.

Figure 7 shows the experimental times to rupture, t_r , under uniaxial creep loading for the nuclear grade type 316 stainless steel studied by Mathew *et al* [34] and Sasikala *et al* [35]. Considerable variation in the experimental times to rupture is observed because the rupture process is intrinsically stochastic. The predicted time to rupture obtained from the present deterministic model is also shown. The predictions are generally in good agreement with the experimentally measured times to rupture except at the highest nominal stress level, $\Sigma_a = 295 \text{ MPa}$. The overestimation of t_r at $\Sigma_a = 295 \text{ MPa}$ possibly points to incipient transition of the dominant rupture mechanism from homogeneous ductile rupture to transgranular cracking [4], which is not accounted for in the present model. In the latter mode, the stress concentration at matrix inclusions determines the rate of damage accumulation.

Creep simulations at each load level are terminated when either the brittle (Section 2.1.3) or ductile (Section 2.2.2) rupture conditions are satisfied. As indicated in Figure 7, rupture is by the brittle mode for $\Sigma_a < 170 \text{ MPa}$ and by the ductile mode for $\Sigma_a > 170 \text{ MPa}$. The observed transition in the failure mode from brittle to ductile agrees with the experimental observations of Sasikala *et al* [35], who observed a dimpled morphology of the fracture surface corresponding to ductile fracture at $\Sigma_a = 295 \text{ MPa}$ and round cavities signifying brittle fracture separated by regions of ductile fracture of

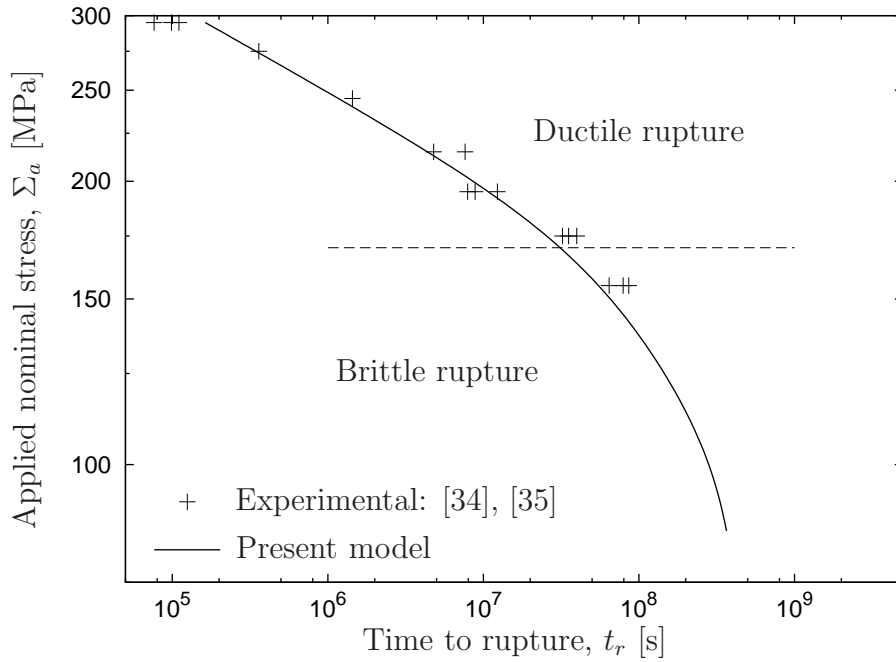


Figure 7. Comparison of the time to rupture under uniaxial creep loading for a type 316 stainless steel obtained experimentally (+) by [34, 35] and computation based on the present model (line).

ligaments at $\Sigma_a = 145$ MPa. The transition of the failure mode from brittle to ductile is, however, not sharp in that considerable damage in the form of wedge-cracking and cavitation occur even in the ductile stress range for $\Sigma_a \gtrsim 170$ MPa. Similarly, for $\Sigma_a \lesssim 170$ MPa, considerable macroscopic specimen extension occurs even in the brittle stress range, as will be shown below. It may therefore be more meaningful to refer to a transitional stress range where the failure mode switches gradually from brittle to ductile.

The maximum principal stretch of the representative grain in the present model, λ_1 , defined in Section 2.2.2 at rupture is shown in Figure 8. Because by definition, $\lambda_1 \uparrow \infty$ in the ductile rupture regime, the maximum principal stretch is meaningful only in the brittle regime. The applied stress range, Σ_a (abscissa) in Figure 8 is therefore restricted to the brittle regime, $\Sigma_a < 170$ MPa. Figure 8 shows that the principal stretch increases drastically as the ductile regime is approached. The experimental elongations observed by Sasikala *et al* [35] at 873 K are too noisy for quantitative comparison with the present predictions. However, the increasing trend of λ_1 with Σ_a observed here is qualitatively confirmed by their measurements.

We now turn to the predicted evolution of microscopic damage. As shown in Figure 1, the orientation of the idealized grain relative to the applied loading is such that facets 5 – 12 are symmetrically disposed relative to the loading. Since facets 1 and 3 are normal to the applied load, no sliding systems are activated in these facets. Therefore, no sliding induced cavitation occurs in them. Any cavitation in these facets

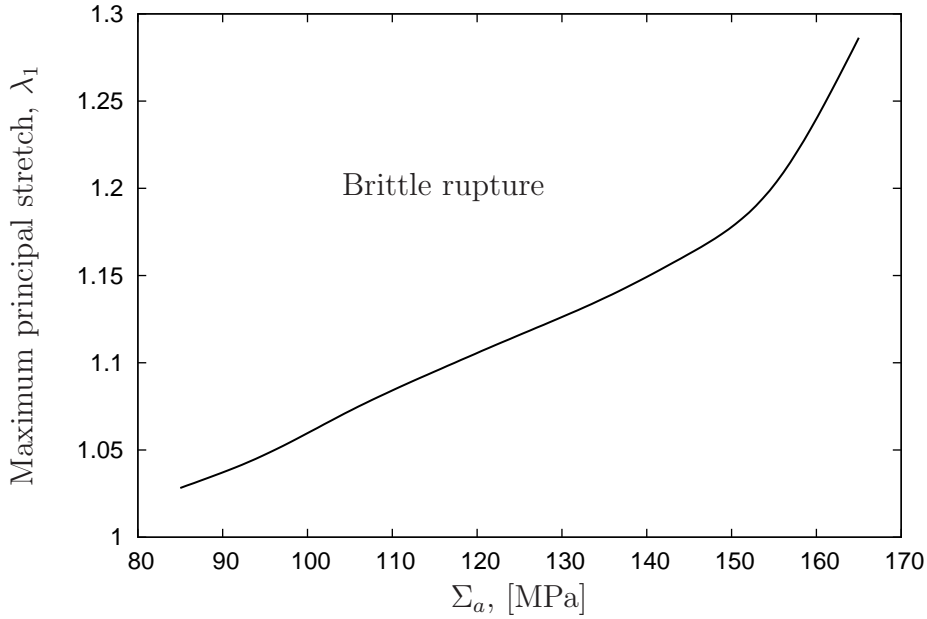


Figure 8. The maximum principal stretch of the representative grain in the present model, λ_1 at rupture. Since $\lambda_1 \uparrow \infty$ in the ductile regime, the applied stress range, Σ_a (abscissa) in Figure 8 is confined to the brittle regime.

must occur by a mechanism of diffusion only. Grain boundary sliding, however, occurs in facets 5 – 12 and induces both diffusional and grain boundary induced cavitation therein. It also induces wedge cracking in facets 1 and 3. Facets 2 and 4 are oriented such that neither grain boundary sliding nor wedge cracking occurs in them.

Damage evolution of facets 1 and 3 and that on facets 5 to 12 are equivalent. Facets 2 and 4 remain undamaged throughout. It therefore suffices to study damage evolution on a representative facet from each of the two damaging groups, chosen as facets 1 and 5. Figures 9 (a) – (d) show the damage evolution in facet 1 and Figures 9 (e) – (h) show the same in facet 5. Rows correspond to applied stress $\Sigma_a = 225$ MPa, 175 MPa, 125 MPa and 85 MPa, respectively. The first two stress levels considered fall in the ductile rupture regime, while the last two stress levels fall in the brittle rupture regime.

As noted above, facet 1, lacking any grain boundary sliding, undergoes creep damage by diffusional cavitation and by wedge cracking. The former is indicated by the curves labeled $\sum_{s \in \mathcal{S}_1} \hat{l}_s$ and the latter by the curves labeled $\sum_{c \in \mathcal{C}_1} \hat{L}_c$, in Figures 9 (a) – (d). The total damage in facet 1, ϕ_1 , which is the sum of these two contributions pulled back into the reference configuration is also shown. Similarly, facet 5 undergoes cavity extension by mechanisms of diffusional growth and grain boundary sliding. Normalized sliding displacement is labeled $\sum_{s \in \mathcal{S}_5} \hat{S}_s$ and normalized cavity length by $\sum_{s \in \mathcal{S}_5} \hat{l}_s$, regardless of whether cavity growth occurs due to diffusion or sliding in Figures 9 (e) – (h).

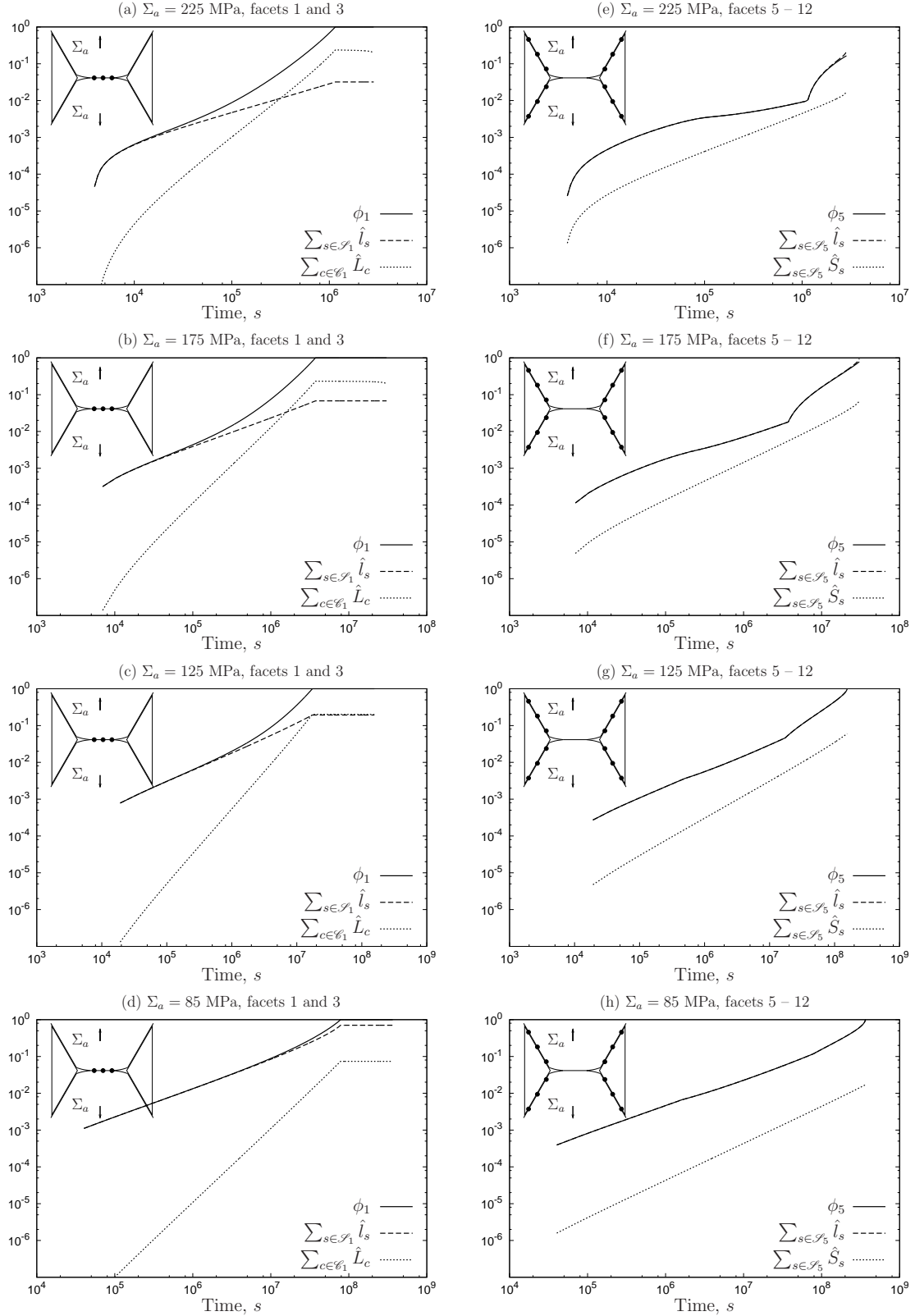


Figure 9. Damage evolution in the form of cavitation and wedge cracking on facets normal (a) – (d) and inclined (e) – (h) to the tensile direction. Rows correspond to different applied normal stresses, $\Sigma_a = 225$ MPa, 175 MPa, 125 MPa and 85 MPa.

The relative contribution of the two damage mechanisms – diffusional cavitation and wedge cracking – varies with applied stress Σ_a . At $\Sigma_a = 225$ MPa and 175 MPa, as seen from Figures 9 (a) and (b), damage caused by wedge cracking dominates that due to diffusional cavitation at the time of rupture of facet 1. At $\Sigma_a = 125$ MPa, as seen from Figure 9 (c), the contribution from both mechanisms is nearly equal and at $\Sigma_a = 85$ MPa, the contribution from diffusional cavitation far exceeds that from wedge cracking. In qualitative agreement with experimental observations [35], the present model predicts an increasing prominence of wedge cracks with increasing applied stress Σ_a .

The last part of each curve in Figures 9 (a) – (d) is flat. This portion corresponds to the time range wherein facets 1 and 3 are fully damaged but facets 5 – 12 are not. The presence of the flat portion in all three plots indicates that the facet normal to the applied load damages fully before any of the inclined facets. Damage evolution of facet 5 does not go to completion in Figures 9 (e) and (f) because creep rupture in this case occurs by the ductile mode.

Facets 5 – 12 are inclined to the tensile direction and undergo grain boundary sliding. The extent of grain boundary sliding at rupture decreases with decreasing stress in the cases depicted in Figures 9 (f) – (h). Creep damage in these facets occurs by diffusional and grain boundary sliding induced cavitation. Wedge cracking does not occur in these facets.

Curves depicting the evolution of cavities in facet 5, $\sum_{s \in \mathcal{F}_5} \hat{l}_s$ in Figures 9 (e) – (g) show a kink at the time that facet 1 becomes fully damaged. The kink is caused by a pronounced reduction in cavity growth rate on the sliding facets prior to complete rupture of the facets 1 and 3. During this period, according to (45), the energy associated with the hollow dislocation at the triple junction suppresses cavity growth. Once the facets normal to the loading direction are fully damaged, the hollow dislocation vanishes [22]. Grain boundary sliding induced cavitation becomes considerably accelerated thereafter. The transition from cavity suppression to cavity growth acceleration is abrupt and produces the kinks in Figures 9 (e) – (g). Figure 9 (h) showing damage evolution on facet 5, however, shows no kink in the $\sum_{s \in \mathcal{F}_5} \hat{l}_s$ curve. This is because, at this low stress level, cavity growth occurs exclusively by the mechanism of diffusion, which, as noted in Section 2.3.2, is uncoupled from wedge cracking.

4. Conclusion

A model of high temperature creep deformation and damage in an austenitic stainless steel polycrystal accounting for creep deformation of grains and simultaneous and coupled damage evolution in the form of cavitation and wedge-cracking at grain boundaries is proposed. Cavitation occurs by a diffusional process at low stress and is driven by grain boundary sliding at intermediate stresses. The model accurately captures the time to rupture of a type 316 stainless steel.

Often in practice, creep-lifetime under service conditions, even if located within the low stress regime dominated by diffusional mechanisms and r-type voiding, is

extrapolated from lifetime data generated by accelerated tests conducted at stress levels extending well into the intermediate stress regime [62], where grain boundary sliding and wedge cracking are dominant. Frequently, extrapolation is based on an empirical time-temperature parameter [63].

The present model based extrapolation scheme offers important advantages over the empirical approach. The model based scheme explicitly represents three damage micromechanisms and predicts their evolution with time. Therefore, in addition to validation against macroscopic creep measures such as the creep curve or time to rupture data, the present model can be validated against microscopic damage measures obtained from quantitative metallographic studies of creep specimen. Model validation can thus be performed at both the macroscale and microscale. Also, once validated, the present model can be used for lifetime predictions in the course of arbitrarily complex loading histories without further approximations or assumptions.

Acknowledgments

We thank the reviewers for many valuable comments that helped to substantially improve this article. Funding for this research was provided by the Indira Gandhi Center for Atomic Research, Kalpakkam.

References

- [1] A. H. Cottrell. Theory of brittle fracture in steel and similar metals. *Trans. AIME*, 212:191–203, 1961.
- [2] J. A. Williams. A theoretical derivation of the creep life of commercial metals failing by triple point cracking. *Phil. Mag.*, 15:1289–1291, 1967.
- [3] H. E. Evans. The growth of creep cavities by grain boundary sliding. *Phil Mag.*, 23(185):1101–1112, 1971.
- [4] D. A. Miller and T. G. Langdon. Creep fracture maps for 316 stainless steel. *Metall. mater. trans.*, 10A:1635–1641, 1979.
- [5] H. J. Frost and M. F. Ashby. *Deformation mechanism maps*. Pergamon press, Oxford, 1982.
- [6] T. J. Chuang, K. T. Kagawa, and J. R. Rice. The shape of intergranular creep cracks growing by surface diffusion. *Acta metall.*, 21:1625–1628, 1973.
- [7] T. J. Chuang, K. T. Kagawa, J. R. Rice, and L. B. Sills. Non-equilibrium models for diffusive cavitation of grain interfaces. *Acta metall.*, 27:265–284, 1979.
- [8] A. C. F. Cocks and M. F. Ashby. On creep fracture by void growth. *Prog. mater. sci.*, 27(3–4):189–244, 1982.
- [9] P. M. Anderson and J. R. Rice. Constrained creep cavitation of grain boundary facets. *Acta metall.*, 33(3):409–422, 1985.
- [10] V. Tvergaard. On the creep constrained diffusive cavitation of grain boundary facets. *J. Mech. Phys. Solids*, 32(5):373–393, 1984.
- [11] V. Tvergaard. Effect of grain boundary sliding on creep constrained diffusive cavitation. *J. Mech. Phys. Solids*, 33(5):447–469, 1985.
- [12] E. Van der Giessen and V. Tvergaard. A creep rupture model accounting for cavitation at sliding grain boundaries. *Int J Fracture*, 48:153–178, 1991.
- [13] E. Van Der Giessen and V. Tvergaard. Development of final creep failure in polycrystalline aggregates. *Acta metall. mater.*, 43(3):959–973, 1994.

- [14] E. Van der Giessen and V. Tvergaard. Micromechanics of intergranular creep failure under cyclic loading. *Acta mater.*, 44(7):2697–2710, 1996.
- [15] N. G. Needham and T. Gladman. Nucleation and growth of creep cavities in a type 347 steel. *Met. Sci.*, 14:64–72, 1980.
- [16] B. F. Dyson. Constraints on diffusional cavity growth rates during creep. *Metal. Sci.*, 10(349–353), 1976.
- [17] J. R. Rice. Constraints on the diffusive cavitation of isolated grain boundary facets in creeping polycrystals. *Acta metall.*, 29:675–681, 1981.
- [18] M. E. Kassner and T. A. Hayes. Creep cavitation in metals. *Int. J. Plasticity*, 19:1715–1748, 2003.
- [19] H. C. Chang and N. G. Grant. Mechanism of intercrystalline fracture. *Trans. Am. Inst. Min. Metall. Eng.*, 206:544–551, 1956.
- [20] R. D. Gifkins. A mechanism for the formation of intergranular cracks when boundary sliding occurs. *Acta metall.*, 4(1):98–99, 1956.
- [21] D. M. R. Taplin and L. J. Barker. A study of the mechanism of intergranular creep cavitation by shadowgraphic electron microscopy. *Acta metall.*, 14(11):1527–1531, 1966.
- [22] H. E. Evans. *Mechanisms of creep fracture*. Elsevier applied science, London, 1984.
- [23] J. K. Lai and A. Wickens. Microstructural changes and variations in creep ductility of 3 casts of type 316 stainless steel. *Acta metall.*, 27:217–230, 1979.
- [24] I.-W. Chen and A. S. Argon. Creep cavitation in 304 stainless steel. *Acta metall.*, 29(7):1321–1333, 1981.
- [25] R. Zauter, F. Petry, H. J. Christ, and H. Mughrabi. High temperature creep behaviour and microstructure development of AISI 304L stainless steel. *Mater. Sci. Eng. A*, 124:125–132, 1990.
- [26] I.-W. Chen. Cavity growth on a sliding grain boundary. *Metall. mater. trans.*, 14A:2289–2293, 1983.
- [27] H. Riedel. *Fracture at high temperatures*. Materials research and engineering. Springer-Verlag, Berlin, 1987.
- [28] A. Chakraborty and J. C. Earthman. Numerical models of creep cavitation in single phase, dual phase and fully lamellar titanium aluminide. *Acta mater.*, 45:4615–4626, 1997.
- [29] P. Onck and E. Van der Giessen. Microstructurally-based modelling of intergranular creep fracture using grain elements. *Mech. mater.*, 26(2):109–126, 1997.
- [30] P. Onck and E. Van Der Giessen. Influence of microstructural variations on steady state creep in 2D freely sliding polycrystals. *Int. J. Solids Struct.*, 34:703–726, 1997.
- [31] E. Van Der Giessen, P. R. Onck, and M. W. D. Van Der Burg. Some effects of random microstructural variations on creep rupture. *Engng. fracture mech*, 57:205–226, 1997.
- [32] P. Onck and E. Van Der Giessen. Growth of an initially sharp crack by grain boundary cavitation. *J. Mech. Phys. Solids*, 47(1):99–139, 1998.
- [33] S. L. Mannan and M. D. Mathew. Structural materials for fast breeder reactor core components. In B. B. Jha, R. K. Galgali, and V. N. Misra, editors, *Futuristic materials*, chapter 11, pages 100–110. Allied publishers, 2004.
- [34] M. D. Mathew, M. Sundararaman, and S. L. Mannan. Dislocation substructure and precipitation in type 316 stainless steel deformed in creep. *Mater. Trans. JIM*, 38:37–42, 1997.
- [35] G. Sasikala, S. L. Mannan, M. D. Mathew, and K. Bhanu Rao. Creep deformation and fracture behavior of types 316 and 316L(N) stainless steels and their weld metals. *Metal. mater. trans*, 31(4):1175–1185, 2000.
- [36] G. Sasikala, M. D. Mathew, K. Bhanu Sankara Rao, and S. L. Mannan. Creep deformation and fracture behaviour of a nitrogen-bearing type 316 stainless steel weld metal. *J. Nuc. Mater.*, 273(3):257–264, 1999.
- [37] S. Latha, M. D. Mathew, P. Parameswaran, K. Bhanu Sankara Rao, and S. L. Mannan. Thermal creep properties of alloy D9 stainless steel and 316 stainless steel fuel clad tubes. *Int. J. Pres. Ves.*

- Pip.*, 85(12):866–870, 2008.
- [38] C. G. Shastry, P. Parameswaran, M. D. Mathew, K. Bhanu Sankara Rao, and S. D. Pathak. Effect of loading history on the threshold stress in the creep deformation of an austenitic stainless steel. *Mater. Sci. Eng. A*, 473(1–2):133–138, 2008.
 - [39] C. A. P. Horton. The interdependence between grain boundary sliding and grain creep deformation. In J. L. Walter, J. H. Westbrook, and D. A. Woodford, editors, *Grain boundaries in engineering materials*, volume 4, pages 355–364. Proc. Bolton Landing Conf., Claitor’s publication division, 1975.
 - [40] D. C. Drucker. Engineering and continuum aspects of high-strength materials. In V. E. Zackay, editor, *High strength materials*, pages 795–833. John Wiley, 1964.
 - [41] J. R. Dryden. On the creep of ceramics due to a viscous grain boundary phase. *J. Mech. Phys. Solids*, 48:2115–2135, 2000.
 - [42] A. F. Wells. *The third dimension in chemistry*. Oxford, London, 1956.
 - [43] H. C. Chang and N. J. Grant. Grain boundary sliding and migration and intercrystalline failure under creep conditions. *Trans. AIME*, 197(305–312), 1953.
 - [44] S. Kishimoto, N. Shinya, and M. D. Mathew. Application of electron beam lithography to study microcreep deformation and grain boundary sliding. *J. mater. sci*, 32(13):3411–3417, 1997.
 - [45] M. E. Gurtin. *An introduction to continuum mechanics*. Academic Press, New York, 1981.
 - [46] N. J. Hoff. The necking and the rupture of rods subjected to constant tensile loads. *J. Appl. Mech.*, pages 105–108, 1953.
 - [47] ASTM, Philadelphia. *Standard Test Methods for Conducting Creep, Creep-Rupture, and Stress-Rupture Tests of Metallic Materials*, 2006.
 - [48] F. K. G. Odqvist. Non-linear solid mechanics, past, present and future. In M. Hetényi and W. G. Vincenti, editors, *Proc. 12th Int. Congress on Applied Mechanics*, pages 77–99. Springer Verlag, 1969.
 - [49] F. H. Norton. *Creep of steel at high temperatures*. McGraw Hill, 1929.
 - [50] W. F. Hosford. *The mechanics of crystals and textured polycrystals*. Oxford University Press, New York, 1993.
 - [51] C. Zener. *Elasticity and anelasticity*. University of Chicago Press, 1948.
 - [52] R. Z. Valiev, V. G. Khairullin, and A. D. Sheikh-Ali. Phenomenology and mechanisms of grain boundary sliding. *Rus. Phy. J.*, 34(3):253–261, 1991.
 - [53] R. Z. Valiev, V. Yu. Gertsman, and O. A. Kaibyshev. Grain boundary structure and properties under external influences. *Phys. stat. solidi*, 97(1):11–56, 1986.
 - [54] R. S. Gates. The role of grain boundary dislocations in grain boundary sliding. *Acta metall.*, 21(7):855–864, 1973.
 - [55] A. I. Pshenichnyuk, V. V. Astanin, and O. A. Kaibyshev. The model of grain-boundary sliding stimulated by intragranular slip. *Phil. mag.*, 77(4):1093–1106, 1998.
 - [56] B.-N. Kim, K. Hiraga, K. Morita, H. Yoshida, and B.-W. Ahn. Viscous grain-boundary sliding with rotating particles or grains. *Acta mater.*, 57(19):5730–5738, 2009.
 - [57] T. Watanabe. Grain boundary sliding and stress concentration during creep. *Metall. mater. trans.*, 14A:531–545, 1983.
 - [58] P. W. Davies and R. Dutton. Cavity growth mechanisms during creep. *Acta metall.*, 14(9):1138–1140, 1966.
 - [59] J. F. Besseling and E. Van der Giessen. *Mathematical Modelling of Inelastic Deformation*. Chapman and Hall, 1994.
 - [60] J. A. Williams. A general approach to creep failure resulting from wedge crack growth. *Phil. Mag.*, 17:635–639, 1969.
 - [61] K. Radhakrishnan and A. C. Hindmarsh. Description and use of lsode, the livermore solver for ordinary differential equations. In A. C. Hindmarsh, editor, *Lawrence Livermore National Laboratory*, pages 1–124. NASA reference publication, USA, 1993.
 - [62] A. Mendelson, E. Roberts, and S. S. Manson. Optimization of time-temperature parameters for

creep and stress rupture, with application to data from german cooperative long-time creep program. Technical Report D-2975, NASA, 1965.

- [63] F. R. Larson and J. Miller. A time-temperature relationship for rupture and creep stress. *Trans. ASME*, 74(5):765–771, 1952.